Biofabrication

OPEN ACCESS

RECEIVED
23 September 2025

REVISED
10 March 2026

ACCEPTED FOR PUBLICATION
17 March 2026

PUBLISHED
27 March 2026

PAPER

Biomechanical 3D tumor models on a micro-milled high-throughput force sensor array

Bashar Emon[1,10], Ahmadreza Kashefi[1,10], Md Habibur Rahman[1,10], Darbaz Adnan[2], Natalia Ospina-Munoz[1], Seamus M Mellican[1], Sophia Santiago[3], William C Drennan[1], Md Saddam Hossain Joy[1], Aja A Phan[1], Tasmia Afrin[1], Luca S Santovito[7], Bumsoo Han[1,9], Kyle C Smith[1,4,5,6,*], Faraz Bishehsari[2,7,8,*] and M Taher A Saif[1,5,9,*]

[1] Department of Mechanical Science and Engineering, Grainger College of Engineering, University of Illinois Urbana-Champaign, Urbana, IL 61801, United States of America
[2] Rush Center for Integrated Microbiome and Chronobiology Research, Rush University Medical Center, Chicago, IL 60612, United States of America
[3] Department of Health and Kinesiology, College of Applied Health Sciences, University of Illinois Urbana-Champaign, Urbana, IL 61801, United States of America
[4] Department of Materials Science and Engineering, Grainger College of Engineering, University of Illinois Urbana-Champaign, Urbana, IL 61801, United States of America
[5] Beckman Institute for Advanced Science and Technology, University of Illinois Urbana-Champaign, Urbana, IL 61801, United States of America
[6] Computational Science and Engineering Program, Grainger College of Engineering, University of Illinois Urbana-Champaign, Urbana, IL 61801, United States of America
[7] Gastroenterology Research Center, Division of Gastroenterology, Hepatology & Nutrition, Department of Internal Medicine, University of Texas Houston, Houston, TX 77030, United States of America
[8] MD Anderson Cancer Center-UTHealth Houston Graduate School of Biomedical Sciences, Houston, TX, United States of America
[9] CZ Biohub Chicago, LLC, Chicago, IL, United States of America
[10] Equal contributing authors.
[*] Authors to whom any correspondence should be addressed.

E-mail: kcsmith@illinois.edu, faraz.bishehsari@uth.tmc.edu and saif@illinois.edu

Keywords: biomechanics, cancer, high-throughput, 3D tumor, stiffness, force sensor

Supplementary material for this article is available online

Abstract

The tumor microenvironment plays a critical role in drug resistance, with extracellular matrix mechanics, cell-cell crosstalk, and transport barriers contributing to poor therapeutic outcomes. Traditional two-dimensional (2D) cultures fail to capture these features, and drug efficacy in 2D often does not translate to three-dimensional (3D) models or *in vivo* tumors. Here, we present a 3D tumor model integrated with a high-throughput biomechanical sensor array that enables simultaneous measurement of cellular forces and matrix remodeling. The platform, fabricated using a scalable and cost-effective micro-milling approach, supports the parallel generation of multiple tumor constructs within a single dish. To demonstrate feasibility, we formed *in vitro* tumors using patient-derived pancreatic ductal adenocarcinoma organoids, cancer cells, and stromal fibroblasts. The sensors were then applied to characterize the evolving biophysical properties of these tumors (tissue force and stiffness) and to evaluate responses to chemotherapy drug, Gemcitabine, and the investigational agent, all-trans retinoic acid. Drug responses in 3D tumors were compared with those in 2D cultures. By combining biochemical and biomechanical readouts, this 3D platform provides a more physiologically relevant tumor model and a powerful tool for preclinical drug testing and personalized medicine.

1. Introduction

Traditional two-dimensional (2D) culture systems have been instrumental in cancer research and drug development, but they poorly recapitulate the complexity of *in vivo* tumor microenvironment [1]. In contrast, three-dimensional (3D) tissue models provide more physiologically relevant cell-cell and cell-matrix interactions, and therefore hold greater promise for drug screening and personalized medicine [2, 3]. One major reason for this discrepancy is that 3D tissues preserve mechanical and structural features of the tumor microenvironment such as matrix stiffness, cell-generated forces, and dynamic cell-matrix crosstalk that profoundly affect drug penetration, signaling pathways, and therapeutic efficacy [4–6]. These biomechanical interactions, absent in 2D cultures, highlight the need for methods that can directly measure forces and mechanical remodeling in 3D models. However, while current 3D models capture biological and biochemical aspects, mechanobiological properties remain underutilized as facile and precise measurement of cellular forces within 3D extracellular matrices (ECMs) have been a long-standing challenge [7–12]. Moreover, existing platforms that can measure such forces are often low-throughput and technically complex, limiting their scalability for systematic studies or clinical applications. Thus, there remains a critical need for accessible, high-throughput tools that integrate biomechanics into 3D disease models.

To address this, we introduced a 3D tumor model, integrated with a biomechanical sensor, that enables simultaneous probing of biochemical and biomechanical parameters, providing a comprehensive view of how cellular forces, matrix stiffness, and remodeling contribute to therapeutic response in 3D tumor models. The system is capable of quantifying: i) the force exerted by cells within 3D matrices and ii) the stiffness of the cell-matrix environment over time to assess matrix remodeling by the cells [13, 14]. This sensor circumvents the assumption of constitutive relations by using force balance to measure traction forces generated by small cell clusters in complex matrices. The sensors are made of polydimethylsiloxane (PDMS) cast from a microfabricated silicon mold [13, 14]. Despite its successful implementation in research labs, the sensor's relatively high cost and complexity have limited its widespread clinical adoption [15–17]. To enhance the sensor's adaptability and ease of use, here we developed a high-throughput sensor array fabricated with PDMS using low-cost micro-milled polymethylmethacrylate (PMMA) molds. Compared to previous methods [7, 13, 18], this array of sensors facilitates generation of multiple replicates with a substantially faster workflow, enhancing versatility and enabling exploration of new avenues for applications beyond fundamental research, including potential integration into hospital drug screening protocols for individualized medicine by enabling the observation and quantification of critical biophysical features of the tumor microenvironment, including diffusivity, alongside the assessment of cellular biochemical signaling and viability, thereby providing valuable insights into its therapeutic relevance.

This innovative fabrication approach offers several advantages over other methods such as deep reactive ion etching (DRIE) or stereolithography [19]. Firstly, it allows the simultaneous generation of numerous samples within a single dish in a high throughput fashion, facilitating the exploration of diverse culture conditions. Secondly, micro-milling of PMMA significantly reduces production costs and time compared to traditional silicon microfabrication techniques like DRIE [19–22]. Thirdly, micro-milling enables greater depth of cutting and offers a larger space compared to etching silicon wafers with limited dimensions. Finally, milling techniques are capable of creating variable depth and 3D structures without any additional steps. In contrast, DRIE requires multiple etching steps and masks to achieve similar complexity and depth, which can increase the time and cost of the fabrication process. The main limitation of micro-milling, compared to DRIE, is its precision and resolution. However, the precision of micro-milling is comparable to that of 3D printing, making it a viable option for applications requiring moderate to high resolution. The high-throughput device, fabricated using micro-milled PMMA molds, combines cost-effectiveness, precision, and the ability to generate multiple replicates simultaneously. This approach significantly lowers production costs and enhances accessibility to advanced biomechanical tools. Despite the limitations in resolution, the benefits of reduced cost, space, depth of cut and three-dimensionality make micro-milling a promising method to fabricate precision equipment for testing biomaterials and cell/tissue mechanics. To demonstrate such capabilities, we utilized *in vitro* cancer tumors as a model system, since the dynamic interplay between cellular forces and the tumor microenvironment plays a critical role in cancer progression [23–28]. This approach allowed us to showcase the device's ability to measure biomechanical parameters, such as contractility and matrix remodeling, providing valuable insights into cancer mechanobiology.

To demonstrate the utility of this platform beyond fabrication, we employed our high-throughput sensor array to probe the mechanobiology of 3D tumor tissues under drug treatment. Specifically, we tested the effects of all-trans retinoic acid (ATRA)

and Gemcitabine in patient-derived pancreatic ductal adenocarcinoma (PDAC) organoids. The platform allowed us to monitor drug-induced changes in contractility and matrix remodeling over time within the 3D constructs. These biomechanical readouts provide an added dimension of insight compared to conventional viability-based assays, highlighting the importance of integrating mechanics into drug testing and discovery.

2. Results

2.1. Concept: 3D tumor model assembled on a mechanical sensor

The unit sensor, housing a single *in vitro* tumor, is designed based on our previous work [13]. In concept, the sensor consists of three main components: a soft spring, a stiff spring, and two grips connected to the springs (figure 1(A)). The soft spring is the force sensor, and the stiff spring stabilizes the 3D tumor specimen that self-assembles *in situ* from a capillary bridge made with cell-ECM mixture between the grips (figure 1(A)). When cells generate contractile force F, it deforms the soft spring by δ_f, thus producing a force readout from the sensor of $F_{readout} = K_f * \delta_f$. In addition, by stretching or compressing the specimen, we can measure the mechanical properties (e.g. stiffness, elastic or visco-elastic moduli) of biomaterials and matrices. We designed the springs as cantilever frames made of PDMS (figure 1(A)). The spring frame, consisting of thin beams, is designed and anchored at one end so that the other end (connected to the specimen) can translate along the length of the tissue sample. The spring constant for n beams is $K_s = {}^{12nEI}/_{L^3}$; where E is the modulus of elasticity of PDMS, I is the moment of inertia ($I = {}^{hb^3}/_{12}$, with b and h being the width and depth of the beams), and L is the length of the beams.

In order to understand the relationship between the force applied by the cell(s) within the matrix (F) and the force detected by the sensor ($F_{readout}$), it is important to consider how the applied force is transmitted to the sensor spring. For example, a specimen with muscle cells forms bundles of myotubes that are attached to the grips on both ends (figure 1(B)). Such muscle tissues apply contractile force directly to the sensor springs through the grips and the total force generated by the muscle is $= (K_f + K_{tissue,c}) * \delta_f$, where $K_{tissue,c}$ is the stiffness of the tissue in compression. Typically, $K_{tissue,c} \ll K_f$, to produce an applied force $F \approx K_f * \delta_f = F_{readout}$. Similarly, for neuronal tissues (figure 1(C)), where cells are confined within the grips and neuritis connect in the central region, force is applied directly on the force sensing spring which precisely detects the applied force. Here, $F = (K_f + K_{matrix,c}) * \delta_f$, where $K_{matrix,c}$ is the stiffness of the matrix in compression. Again, when $K_{matrix,c} \ll K_f$ is satisfied, $F \approx F_{readout}$ is produced.

In specimens with single cells (figures 1(D) and (E)), the cells apply force on the matrix that transmits the force to the springs. When the cell is located at the center (figure 1(D)), the matrix within the force dipole is under compression. Matrices such as collagen are composed of thin fibers (~0.1–1 μm [29]) that are strong in tension but buckle under small compressive stress. Therefore, any force on collagen is transferred almost entirely to the sensor's spring by tension (figure 1(F)). It should be noted that a small fraction of the applied force is used to buckle collagen fibers, and this fraction is not transferred to the sensor spring, even for cases where the cell is adhering to the grips at one end (e.g. figure 1(E)) [14].

The sensor also enables mechanical testing of the specimens allowing for the measurement of mechanical properties such as elastic modulus or stiffness [13, 14]. As illustrated in figure 1(A), the method for assessing tissue stiffness involves stretching or compressing the tissue sample by moving the stiff spring with a 3D linear stage equipped with micrometers or piezo actuators. The change in length due to compression or tension, along with the corresponding force readout from the soft spring, provides information to determine the tissue's stiffness. For a linear force-displacement response, tissue stiffness can be calculated directly. In cases where the relationship is non-linear, the force-deformation curve is fitted to an appropriate non-linear model to determine the tissue stiffness.

2.2. Micro-milling for the fabrication of sensors with intricate structures

Leveraging recent progress in precision micro-milling technology [19], we investigated the feasibility of fabricating micron-scale structures and components that comprise the biomechanical sensors. We fabricated PMMA molds for the components of the high-throughput sensor system (figure 2(A)). We employed two different methods to make the PMMA molds- direct and indirect milling. Direct milling uses end-mills with diameters smaller than the smallest feature in the design, creates grooves in the form of sensors and the device parts are cast directly from the PMMA mold (figure 2(B)). On the other hand, indirect milling can utilize larger end-mills to create an inverted model of the design (i.e. ridges in the shape of sensors) by cutting out the surrounding material (figure 2(C)). A secondary mold is then cast with PDMS from the PMMA model and then silanized with chlorotrimethylsilane to prevent adhesion with PDMS cured in contact (figure 2(D)). These molds are used to cast PDMS into arrays of sensors.

The performance of the fabricated sensor components using these micro-milling techniques

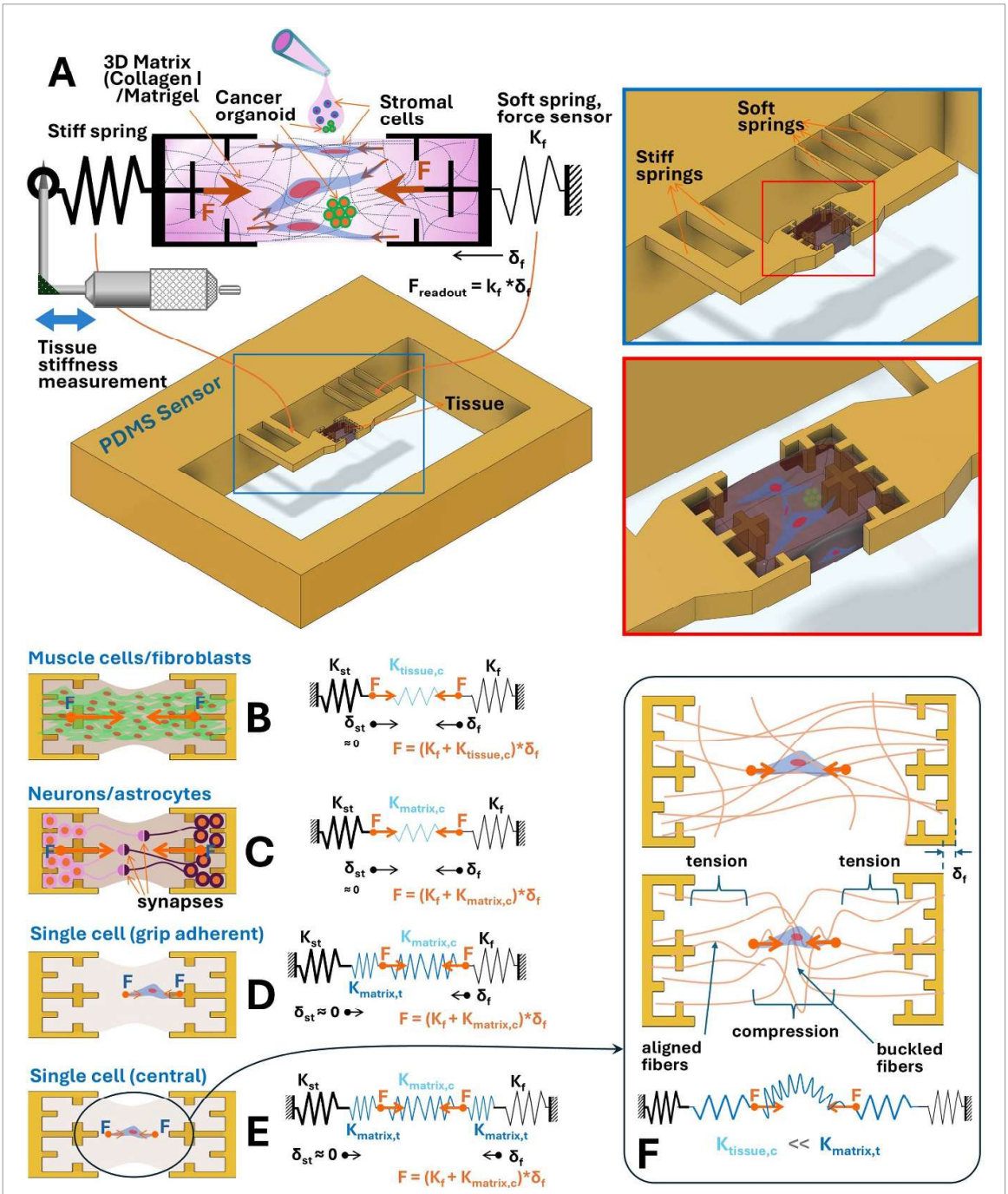

Figure 1. Concept and design of a sensor for measuring cell generated force in 3D matrices and tissue stiffness. (A) Schematic illustration of specimen formation and working principles of the sensor. The tissue sample self-assembles on the sensor from a capillary bridge of cell-ECM mixture between the grips. Over time, the cells activate, interact with the ECM fibers, and generate contractile forces, which are transferred to and deform the soft spring (with a spring constant of K_f). Spring deformation and cellular activity are monitored using a microscope. Cell force is determined by multiplying the spring constant by the deformation ($K_f * \delta_f$). Tissue stiffness is measured by applying axial compression or tension on the specimen with a micrometer attached to a stiff beam, while spring deformation and grip movement are continuously tracked to measure force and strain. For the PDMS sensor, soft springs are designed as thin beams, and wide beams represent stiff springs. Force transmission mechanism in tissues with (B) high density muscle cells or fibroblasts, (C) neurons connected to both grips, (D) single cell located at the center, and (E) single cell adherent to one grip. For cases in (B), (C), $F = (K_f + K_{tissue,c}) * \delta_f \approx K_f * \delta_f$ as $K_{tissue,c} \ll K_f$. For cases in (D), (E), $F = (K_f + K_{matrix,c}) * \delta_f \approx K_f * \delta_f$ as $K_{matrix,c} \ll K_f$. (F) *For cases where regions of the matrix are under compression (e.g. (D) and (E)), fibers within the matrix buckle under small compression, and thus* $K_{matrix,c} \ll K_{matrix,t}$. Therefore, the force readout from the sensor, $F_{readout} = K_f * \delta_f$ is a precise estimate of cell-generated force.

exhibits distinct characteristics. Direct milling often results in wall slopes and achieving a beam width smaller than 80 μm is challenging since smaller end-mills easily break while cutting hard PMMA. Additionally, the maximum aspect ratio (height/width of beams) attainable with direct milling is approximately two, which limits the height of the features relative to their width.

In contrast, with indirect milling, it is possible to achieve a beam width as small as 50 μm, and

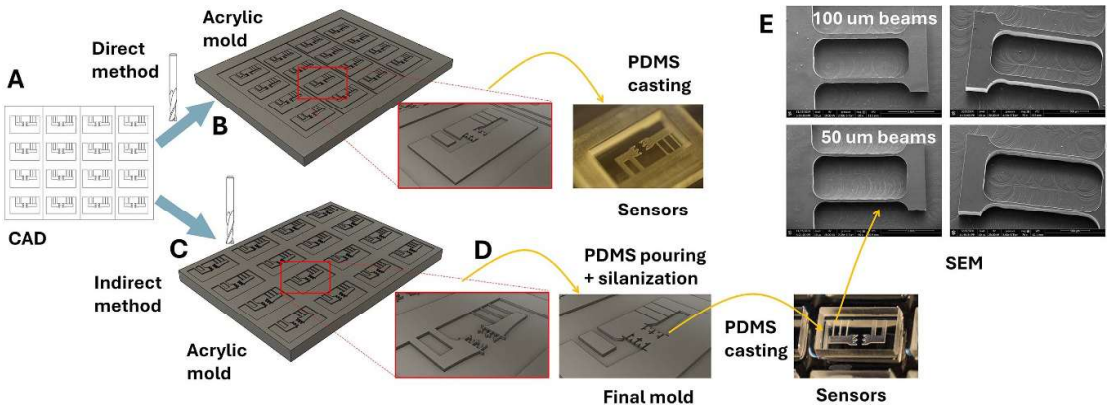

Figure 2. Direct and indirect molding techniques in creating structures and components for biomechanical sensors. (A) The design can have an array of devices in a wide range of dimensions, up to the scale of a 96-well plate, (B) Schematic illustrating the direct molding method by micro-milling a PMMA mold and casting PDMS sensors from this mold. The force sensor arrays used in this study were fabricated using this method. (C), (D) Schematic illustrating the indirect molding method. A positive mold is created by micro-milling of PMMA. By pouring PDMS on the positive mold, curing, removing and silanizing, the final negative mold is created. PDMS sensors are cast on this mold. (E) Scanning electron microscope images of 100 μm beams and 50 μm beams fabricated using indirect micro-milling method.

a remarkable aspect ratio of up to fifteen, allowing for the creation of much taller features relative to their width (figure 2(E)). Moreover, the sidewalls produced through indirect milling are nearly vertical, contributing to more precise and defined cross-sections (figure 2(E)). Another advantage of indirect milling is that the cutting volume is smaller when fabricating molds of sensor arrays. As a result, it takes less time to complete, making it a more efficient process. Furthermore, molds created using this technique can be utilized to make many replicates of the sensor array in PDMS, since PMMA resists wear for repeated use. Therefore, Tool wear and machining time are no longer significant concerns with this approach, as each mold only needs to be machined once.

However, a key limitation is that the gap between beams cannot be made smaller than the size of the tool bit used, which may restrict the design possibilities for certain applications. These differences in performance make indirect milling a more suitable choice for applications requiring high aspect ratios, finer resolution, and faster fabrication times, whereas direct milling is more appropriate for simpler designs with lower aspect ratio requirements.

2.3. Assembly and operational setup

To make a functional high-throughput system from the micro-milled molds, we fabricated an array of precision sensors (figures 3(A) and (B)) and the top/bottom layers (figure 3(C)) that create independent wells for each sensor. The sensor layer is sandwiched between the top and bottom layers and attached to a glass slide to construct the functional high-throughput device (figures 3(C)–(E)). The components are joined with PDMS to ensure a proper seal that prevents leakage and contamination between the wells.

Figure 4 illustrates the process and outcomes of forming tissues on a sensor array. To enhance the sensor's attachment with the matrices (e.g. collagen), the surfaces are treated with (3-aminopropyl)triethoxysilane (APTES) and glutaraldehyde, which improve hydrophilicity and enhance the bond between the grips and the ECM (figure 4(A)). This surface treatment also facilitates the flow of ECM into the micro-channels on the grips improving mechanical anchoring. Tissues are created by forming capillary bridges between the grips using a cell-ECM mixture, which self-assembles into structured tissues upon polymerization (figure 4(B)). Brightfield (BF) microscopy verified the successful formation of sixteen tissue samples, comprising collagen I and pancreatic stellate cells (PSCs), distributed across a 4 $\times$ 4 sensor array (figure 4(C)). Subsequent second harmonic generation (SHG) imaging provided insights into collagen organization within the tissues (figure 4(D)). The analysis revealed that PSCs significantly remodel collagen, as evidenced by increased SHG signal intensity (figures 4(E)) and a pronounced alignment of collagen fibers across the grips (figure 4(F)), underscoring their role in ECM remodeling.

3. Research and clinical applications

3.1. 2D drug-response data indicate that co-culture reduces drug efficacy

The mechanical properties of the ECM support cancer development and contribute to treatment failure and immune evasion, making it a significant target

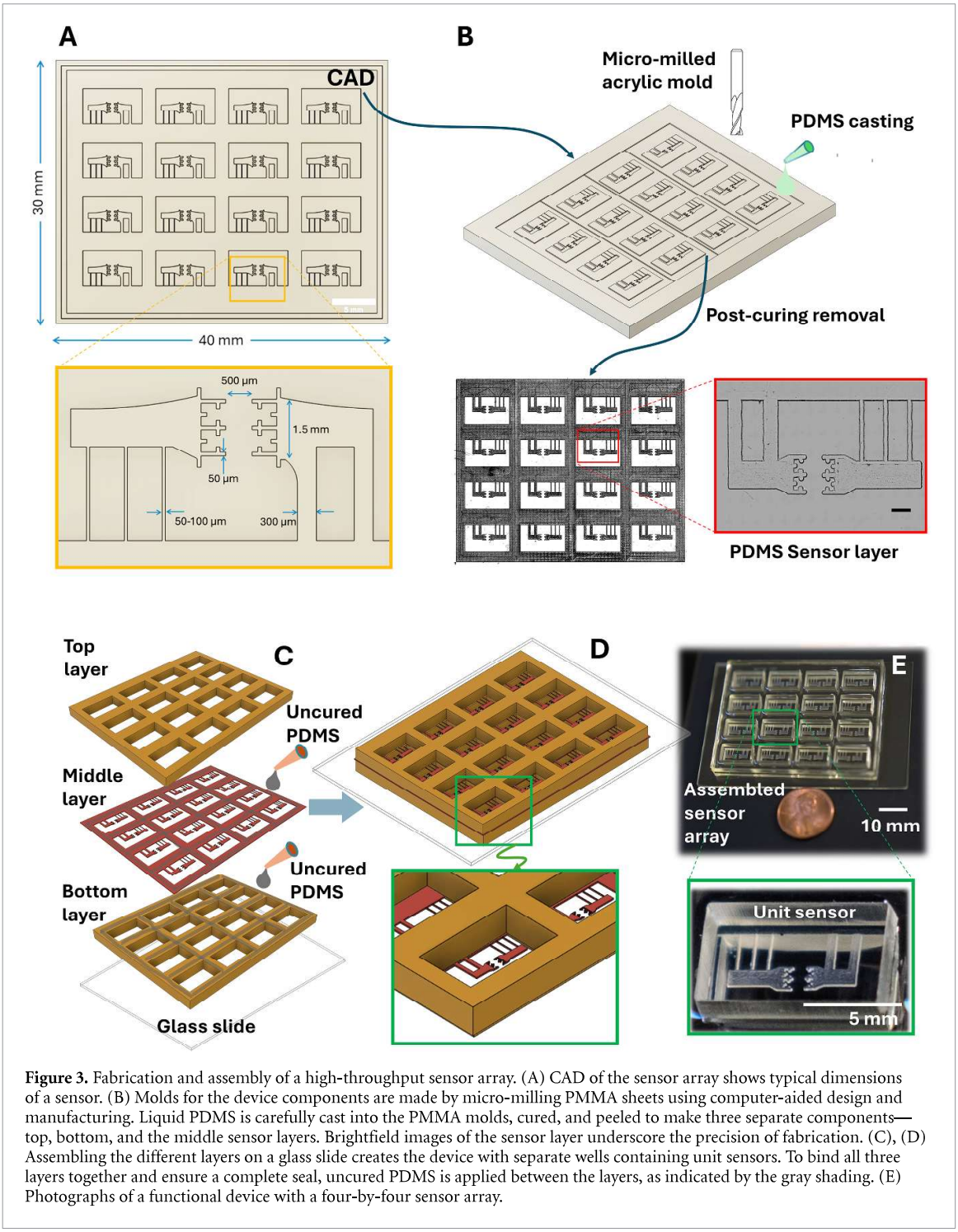

Figure 3. Fabrication and assembly of a high-throughput sensor array. (A) CAD of the sensor array shows typical dimensions of a sensor. (B) Molds for the device components are made by micro-milling PMMA sheets using computer-aided design and manufacturing. Liquid PDMS is carefully cast into the PMMA molds, cured, and peeled to make three separate components—top, bottom, and the middle sensor layers. Brightfield images of the sensor layer underscore the precision of fabrication. (C), (D) Assembling the different layers on a glass slide creates the device with separate wells containing unit sensors. To bind all three layers together and ensure a complete seal, uncured PDMS is applied between the layers, as indicated by the gray shading. (E) Photographs of a functional device with a four-by-four sensor array.

for cancer therapies [16, 23, 24, 30]. Traditional 2D culture models fail to capture these critical mechanical and structural cues, and numerous studies have shown that drug efficacy in 2D often does not translate to 3D models or *in vivo* tumors [31–35]. In contrast, patient-based *in vitro* models, such as 3D tumor spheroids, have advanced our ability to predict drug response. However, better mimics of the complex interactions between the ECM and primary cancer cells are still highly needed. Consistent with previous findings [31–35], our results on PDAC models show that therapeutic responses differ substantially between 2D and 3D, underscoring the relevance of biomechanical context in drug evaluation (figure 5).

To establish the appropriate drug concentrations for assessing cell viability in both 2D and 3D culture systems, we performed half-maximal inhibitory concentration (IC_{50}) assays to determine the cytotoxicity profiles of the drugs (figures 5(A) and (B)). Dose-response to ATRA was examined due to its reported capacity to suppress PSC proliferation and viability and its emerging role as an investigational agent targeting the desmoplastic stroma [36–39]. We determined its IC_{50} as 12.5 μM in inhibiting PSCs viability by

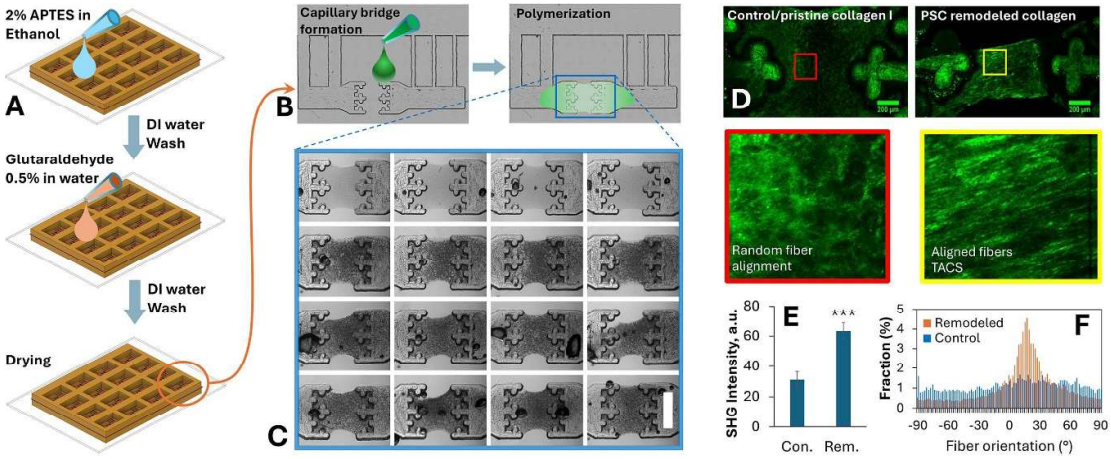

Figure 4. Forming tissues on the sensor array. (A) Sensors are treated with 2% APTES (v/v in ethanol) for 12 h and then 0.5% glutaraldehyde (v/v in water) for an hour, to make the surfaces hydrophilic and to strengthen grip-ECM bonds. (B) Tissue specimens are formed by creating capillary bridges between the grips with cell-ECM mixture that self-assembles into a tissue upon polymerization. (C) Brightfield images of 16 tissue samples (collagen I + pancreatic stellate cells (PSCs) on a single device with 4 × 4 sensors. (D) Second harmonic generation (SHG) images of collagen in an acellular control sample and a PSC tissue, containing only PSCs at a concentration of 660 000 cells ml^{-1}, consistent PSCs count in co-culture experiments. (E) SHG intensity and (F) fiber orientation histogram reveals that PSCs remodel collagen by compaction and fiber alignment.

50% in 2D PSC monoculture (figure 5(A)). In addition, dose-response analysis with MIA PaCa-2 cancer cells indicated an IC_{50} of 250 nM for Gemcitabine (a standard chemotherapeutic agent for pancreatic cancer [40–42]) (figure 5(B)).

We first verified that the reduction in CellTiter-Glo 3D luminescence observed during IC_{50} determination was consistent with the response measured in monocultures treated with Gemcitabine or ATRA at their respective IC_{50} concentrations. Specifically, treatment of 3,300 MIA PaCa-2 cells with Gemcitabine resulted in a ∼19%–20% decrease in luminescence (figure 5(C)), consistent with the ∼19.4% reduction observed during IC_{50} determination (figure 5(B)). Similarly, 1600 PSCs treated with ATRA exhibited a ∼5%–6% decrease in luminescence (figure 5(C)), comparable to the ∼5.2% reduction measured in the IC_{50} assay (figure 5(B)). These results confirm the consistency of experimental readouts (i.e. luminescence) in response to individual and combination of the drugs in both MIA PaCa-2 and PSCs.

Next, we confirmed that the luminescence signal of the untreated co-culture matched the summed luminescence of the corresponding untreated monocultures, verifying that signal contributions from the two cell types are additive (figure 5(D)).

Finally, we compared the summed luminescence reduction of the treated monocultures to the luminescence reduction observed in the treated co-culture. The treated co-culture exhibited a significantly higher residual signal, indicating that the establishment of the co-culture attenuated drug efficacy and resulted in a markedly smaller ATP signal drop relative to the monoculture conditions (figure 5(E)).

3.2. Drug and Biomechanical response in 3D

To assess whether this effect was maintained in 3D cultures, micro-tumor models (co-culture of MIA PaCa-2 and PSCs (2:1 ratio)) were created on the microarray devices and allowed to compact for 24 h prior to treatment. They were then exposed for 24 h to Gemcitabine, ATRA, or Gemcitabine + ATRA at their respective IC_{50} concentrations, with untreated tissues as controls (figure 6(A)). Viability was measured using the CellTiter-Glo 3D assay, after 24 h of tissues being treated with all drug regimens (figure 6(F)). Specifically, there was no statistically significant change in viability due to ATRA, or Gemcitabine alone. Gemcitabine + ATRA reduced viability by about 13.5%.

Utilizing our high-throughput sensor system with cancer models *in vitro* (figure 6), we investigated the biomechanical response of the 3D cancer tissue consisting of MIA PaCa-2 and PSCs to the drugs. To establish a model that recapitulates key features of the pancreatic cancer microenvironment, we developed a co-culture system consisting of pancreatic cancer cells (MIA PaCa-2) and PSCs with 2:1 ratio (figures 6(A)–(E)). The tumor models exhibit uniform distribution of different cells (figures 6(C)–(E)). The cells were allowed to compact for 24 h prior to any treatment. In this setting, cancer cells act as the primary drivers of PSC activation, while PSCs contribute to ECM remodeling, a critical process in pancreatic tumor progression. Within 24 h, PSC-mediated contractile activity generated force (figure 6(G)) and increased scaffold stiffness by approximately 2-fold, indicating ECM remodeling (figure 6(H)).

Drug treatment for 24 h revealed distinct mechanobiological outcomes. Treatment with ATRA, either

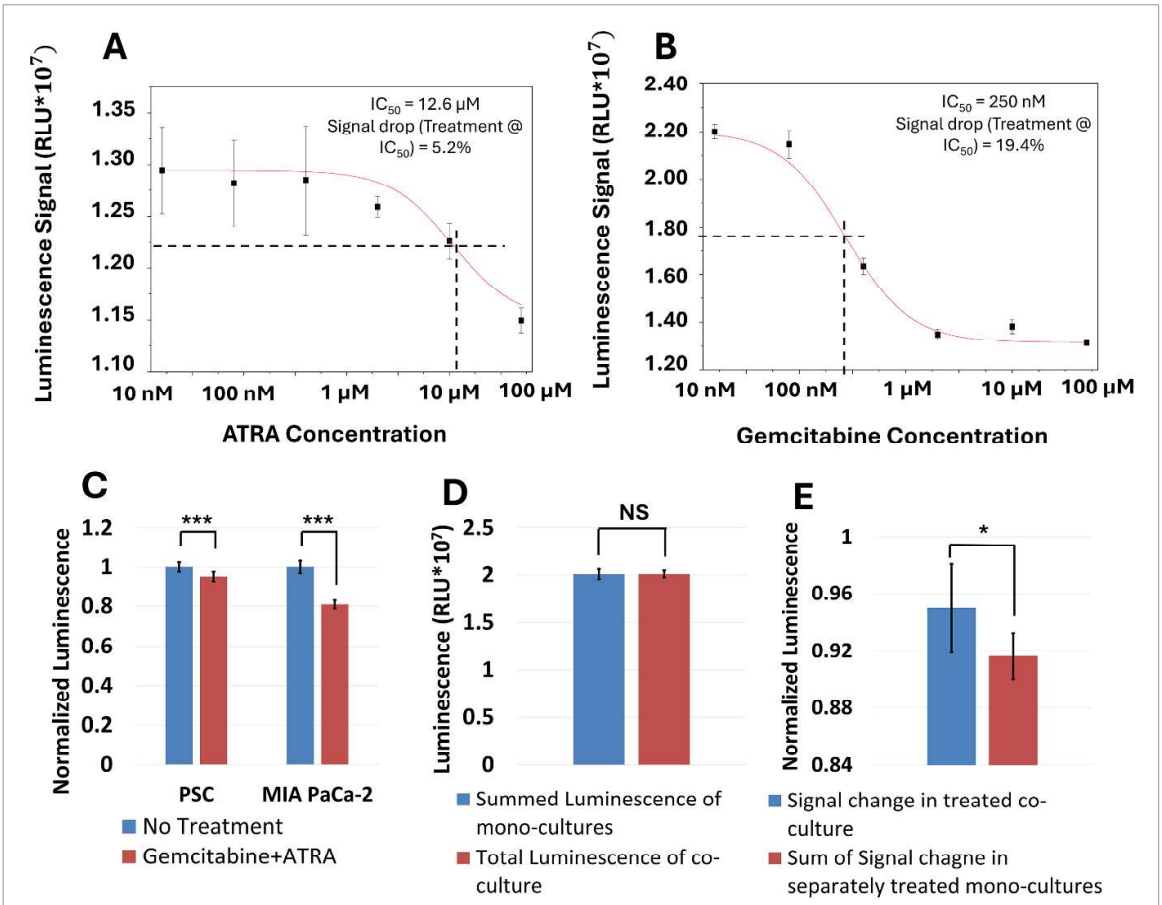

Figure 5. Dose-response of cells in pancreatic cancer cells and stromal fibroblasts in 2D. (A) IC_{50} assay performed on PSC cell line, treated with ATRA. (B) IC_{50} assay performed on MIA PaCa-2 cell line, treated with Gemcitabine. (C) CellTiter-Glo 3D luminescence, normalized to untreated controls, was used to evaluate the effect of combined Gemcitabine and ATRA treatment (at their respective IC_{50} concentrations) on monocultures of 3300 MIA PaCa-2 cells and 1600 PSCs ($n = 10$). This analysis assessed the impact of the combination treatment in the absence of co-culture conditions. (D) Luminescence signal from the untreated co-culture (3,300 MIA PaCa-2 cells + 1600 PSCs) was compared with the summed luminescence obtained from the corresponding untreated mono-cultures seeded at identical cell densities and was found to be comparable ($n = 10$). (E) In contrast, following treatment with drug combination, the luminescence signal measured in the co-culture was significantly greater than the summed signal from the treated mono-cultures of MIA PaCa-2 and PSCs ($n = 10$). In mono-culture conditions, 3300 MIA PaCa-2 cells or 1600 PSCs were seeded per well, whereas co-culture samples contained both cell types at the same respective numbers. Statistical significance was determined by student's T-test ($^{*}p < 0.05$, $^{**}p < 0.01$, $^{***}p < 0.001$). Column plots: mean ± SD.

alone or in combination with Gemcitabine, significantly decreased tumor force (figure 6(G)) and administration of a combination of Gemcitabine and ATRA attenuated matrix stiffness significantly (figure 6(H)). In contrast, Gemcitabine monotherapy failed to induce any significant change in either force or stiffness. These findings suggest that Gemcitabine-ATRA-mediated stromal reprogramming exerts a pronounced influence on the properties of the pancreatic cancer microenvironment, an effect not replicated by Gemcitabine alone.

3.3. Patient-derived 3D PDAC organoids for biomechanical response to chemotherapy

To evaluate the effect of drug treatment on patient-derived organoids (PDOs), we first examined whether combining Gemcitabine with ATRA enhances therapeutic efficacy relative to Gemcitabine alone. Apoptosis was quantified by assessing cleaved caspase-3 (c.c.3) expression in $EpCAM^{+}$ tumor epithelial cells, allowing differentiating between epithelial and stromal populations. PDAC models were generated by co-culturing PDOs with PSCs and treated with vehicle control, Gemcitabine (at its IC_{50} concentration), or a combination of Gemcitabine and ATRA (at their respective IC_{50} concentrations) for 48 h. One-way ANOVA revealed a significant overall treatment effect on the percentage of c.c.3-$^{+}$/$EpCAM^{+}$ epithelial cells ($F(2,6) = 29.3$, $p = 0.0008$). While Gemcitabine alone produced a modest increase in apoptosis, the combination of Gemcitabine and ATRA resulted in a markedly greater apoptotic response. Pairwise comparison using Welch's t-test confirmed that the combination treatment significantly increased epithelial cell death compared to Gemcitabine alone (mean ± SD: 62.6% ± 6.2% vs. 27.8% ± 8.5%; $t = -4.49$, $p = 0.019$) (figure 7(A)).

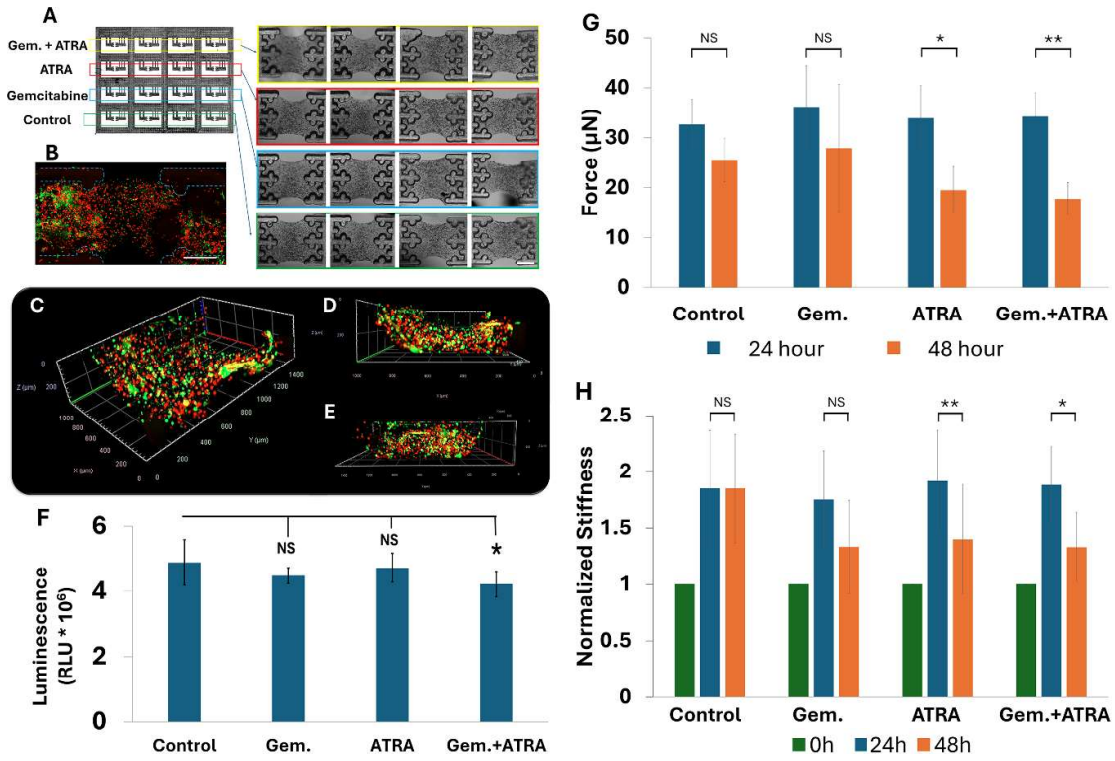

Figure 6. Configuration of 3D co-culture tissues consisting of a co-culture of MIA PaCa-2 and PSCs with a concentration of 1.32 million cells ml^{-1} and 0.66 million cells ml^{-1}, respectively. (A) Experimental setup for drug administration after the initial compaction of the tissues and brightfield (BF) images of tissue specimens containing a co-culture of MIA PaCa-2 and PSCs in 2 mg ml^{-1} of Collagen Type I and 1 mg ml^{-1} Matrigel, before compaction. (B) Fluorescence microscopy image of a tissue, with PSCs marked with Green CellTracker and MIA PaCa-2 cells secreting tdTomato fluorescent protein. (C–D) 3D fluorescence images of the tissue construct between the grips. The tissue was fixed after two hours of tissue formation, and fluorescence confocal microscopy was performed directly after fixation. (C) Isometric and orthogonal views along (D) *X*-axis and (E) *Y*-axis show the 3D distribution of cells. (F) Viability of the cells in 3D tissue shows no significant effect with Gemcitbaine or ATRA monotherapy but a significant decline in viability with the treatment of Gemcitabine + ATRA, with all drug treatments being performed at their IC_{50} concentrations. ($N = 8$). (G) Administration of ATRA alone or in combination with Gemcitabine significantly reduced tumor-generated forces. The blue bars represent forces measured after 24 h of culture without drug treatment, while the orange bars represent forces measured after an additional 24 h of treatment. (H) Matrix remodeling induced by the co-culture was attenuated by ATRA and by the combination of ATRA and Gemcitabine. Tissue stiffness was measured at three time points: 0 h (green bars; baseline stiffness), 24 h (blue bars, after tissue compaction without drug treatment), and 48 h (orange bars, after 24 h of drug treatment). All drug treatments were applied at their respective IC_{50} concentrations, and stiffness values were normalized to the initial stiffness (at 0 h) of each tissue. Statistical significance was determined by one-way ANOVA followed by Fisher's test post hoc ($^{*}p < 0.05$, $^{**}p < 0.01$, $^{***}p < 0.001$). Column plots: mean ± SD. Scale bar: 500 μm.

As force is the key mechanical parameter, we first characterized the forces generated by monocultures of pancreatic cancer cells and PDOs. Samples containing 1.32 million cells ml^{-1} were prepared, and the total contractile forces were measured. Both MIA PaCa-2 cells and PDOs generated forces of approximately ~1 μN (figure 7(B)). Such low force levels are expected, as these epithelial cancer cells exhibit limited intrinsic contractility compared to stromal cells such as fibroblasts. We also measured PSC generated force with samples containing 0.66 million cells ml^{-1}. In contrast to the cancer cell- or PDO-specimens, PSC-only constructs generated forces at 25.2 ± 7.1 μN (figure 7(B)). This large disparity demonstrates that cancer cells or PDOs do not contribute significantly to the force readout in our PDAC biomechanical models, where PDOs are co-cultured with the PSCs (figure 7(C)).

We utilized our high-throughput sensor array to investigate PDAC mechanics *in vitro* (figure 7(C)). PDACs, in general, have an active stroma, with some tumors exhibiting mechanical stiffness up to ten times greater than normal tissue [23, 25, 27]. This pronounced stromal remodeling underscores their potential as models for individualized cancer therapy targeting biomechanics [43, 44].

In our PDAC model, PSCs are the key drivers of stromal remodeling and mechanical stiffening in pancreatic tumors. We found that inclusion of PSCs significantly increased mechanical forces in the PDAC models (figure 7(D)), compared to monocultures. Given that increased force elevates stromal stiffness impairing drug penetration and efficacy, we hypothesized that targeting PSCs with ATRA would reduce tissue contractility and thereby enhance Gemcitabine response. Indeed, combined treatment

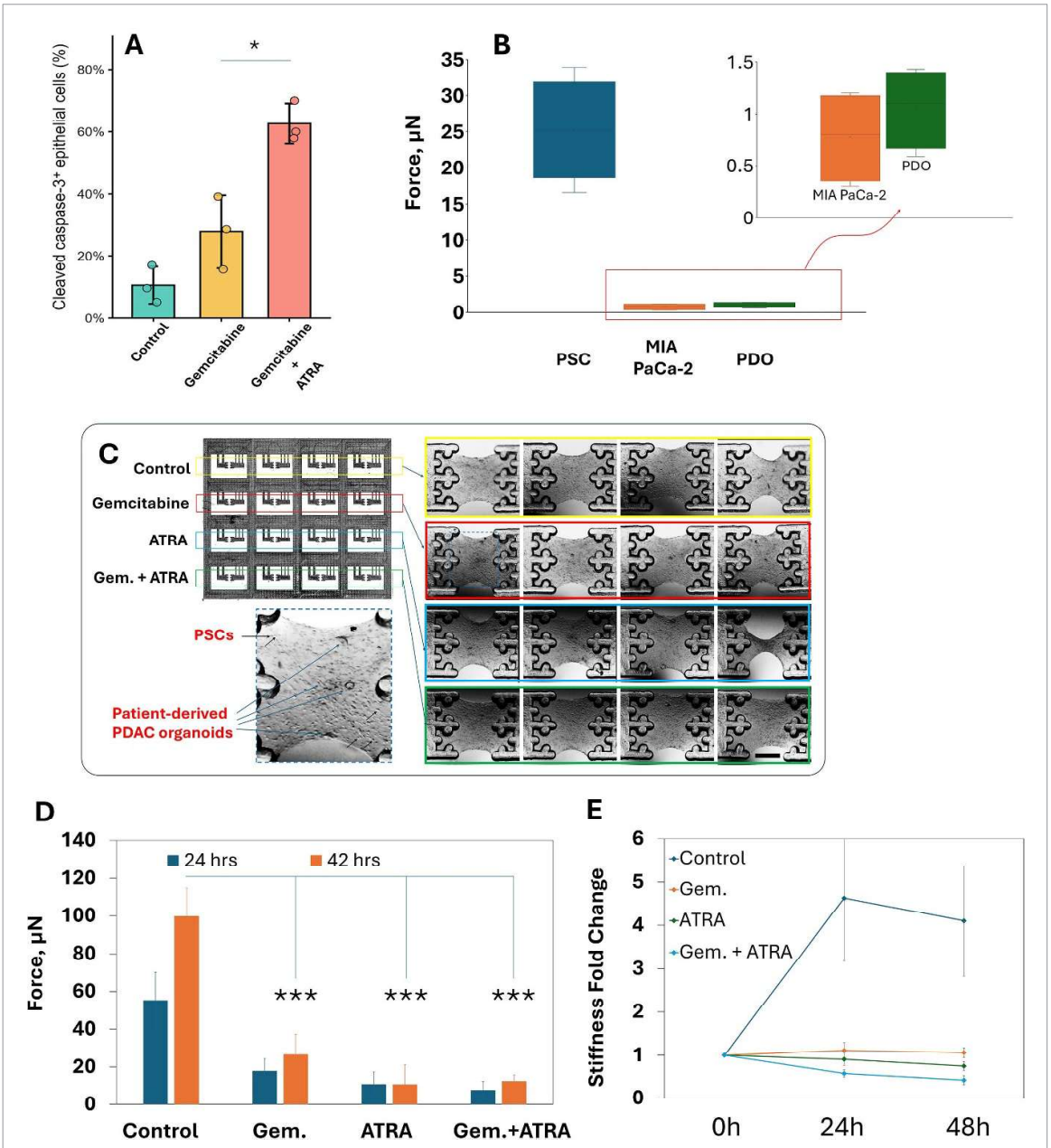

Figure 7. Biomechanical effects of drugs on patient-derived organoids. (A) Organoid viability under chemotherapeutic treatment. Organoids were treated with Gemcitabine or Gemcitabine + ATRA, each applied at its respective IC_{50} concentration. Viability was quantified following treatment. The cancer-on-a-chip platform used for assessing drug efficacy was originally developed by Haque *et al* [43] (B) Mechanical force generated by monocultures of PSC, MIA PaCa-2 and PDOs. (C) Experimental setup for drug administration and brightfield images of *in vitro* PDAC tissues with patient-derived organoids and PSCs. (Inset) Some of the organoids (blue arrows) and PSCs (black arrows) are highlighted. (D) Comparison of tissue force at 24 and 42 h. (E) Change of tissue stiffness in these patient-specific tumor models. Stiffness of the tissues were normalized with respect to Day 1 stiffness of the same sample. Gemcitabine and ATRA both inhibit matrix stiffening and contractility; however, combination treatment is more efficient (statistical significance in table S4 of supplementary information). Error bars: SD. Statistical significance was determined by one-way ANOVA followed by Fisher's test post hoc ($^{*}p < 0.05$, $^{**}p < 0.01$, $^{***}p < 0.001$). Scale bar: 500 μm.

with Gemcitabine and ATRA led to a greater reduction in tissue contractility and stiffness over time compared to either treatment alone (figures 7(D) and (E); table 1). These findings demonstrate that the high-throughput platform can capture both biochemical and biomechanical drug responses and higJ.K.Renhlight its potential utility for mechanics-informed, patient-specific therapeutic testing.

4. Performance comparison and future directions

Despite the significant advancements presented by our high-throughput sensor array, some limitations suggest scope for improvement. While micro-milling offers a cost-effective and scalable alternative to traditional microfabrication methods, our current

Table 1. Biomechanical outputs of drug treatment of *in vitro* PDAC models.

Treatment	Dose	Force	ECM remodeling	Key observations
Control	—	High force sustained at 24 and 42 h	Stiffness progressively increases	Represents baseline with no drug treatment; both contractility and stiffness increase significantly over time (∼400% increase in stiffness**).
Gemcitabine	At IC_{50} concentration	Significant reduction	Stiffening inhibited (i.e. remains unchanged compared to initial)	Inhibits contractility and matrix stiffening significantly (∼70% reduction in contractility*, and complete inhibition of stiffening**).
ATRA	At IC_{50} concentration	Greater reduction	Greater stiffness reduction than Gemcitabine	Stronger inhibition of contractility and matrix stiffening (∼80%–90% reduction in force* and 10%–30% softening of ECM**).
Gemcitabine + ATRA	Both at IC_{50} concentration	Most significant reduction	Most significant reduction in stiffness	The highest efficacy reduction in both contractility and matrix stiffening. (∼80%–90% reduction in force* and 50%–60% softening of ECM**).

*Estimates are made from figure 7(C). Force comparisons are made with respect to the control sample.

**Estimates are made from figure 7(D). Stiffness comparisons at different time points are made with respect to the initial stiffness (0 h) of the same samples. Compared to the control, stiffness reduction with drugs is substantially larger (∼80%–90% lower stiffness compared to control).

technology lacks the ultra-high precision (∼1 μm), particularly when compared to lithographic techniques like DRIE that can achieve feature sizes down to the sub-micron level and aspect ratio of ∼20:1 [45, 46]. In contrast, using micro-milling, we created 50($\pm$5) micron features with a 15:1 aspect ratio. Widely available 3D printers, capable of producing large objects (e.g. 128 mm × 85 mm for a 96-well plate), can achieve the similar features [47]. However, achieving consistent performance for PDMS casting often requires specialty resins, extensive post-processing, and surface treatments to mitigate resin inhibition or leaching, which can increase time and material costs. In this context, micro-milling represents a cost-competitive [19–21] alternative that enables direct fabrication of PDMS-compatible molds with minimal post-processing, making it well suited for scalable, high-throughput biomechanical assays. In addition, it enables deeper structures (depth >1 mm), that are not feasible with DRIE. Moreover, creating 3D features with micro-milling is considerably faster (one-step process) than with lithography, which requires multiple steps adding to time and cost.

Another limitation stems from the constraints associated with using smaller-sized endmills in the micro-milling process. As the diameter of the endmills decreases to achieve finer features, there is an increased susceptibility to tool wear and breakage, which can compromise the dimensional accuracy and consistency of the fabricated sensors. Additionally, smaller endmills require longer machining times, which can lead to thermal effects that potentially distort the PMMA molds. Hence, it is important to use endmills suitable for the instrument and material. Also, the system should have a mechanism for chip removal and temperature control.

There are several avenues for future research and development. One direction is to refine the micro-milling process to enhance the precision of the sensor components, potentially through the integration of advanced milling techniques or hybrid fabrication approaches that combine micro-milling with other high-resolution methods. Another promising direction is the development of more complex tissue models on the sensor array, incorporating multiple cell types, ECM components, and dynamic biochemical gradients to better mimic *in vivo* conditions. This could involve the integration of vascular networks or immune cell populations, providing a more comprehensive understanding of how different cell types

interact within a 3D matrix under various mechanical and biochemical cues.

Furthermore, expanding the application of the sensor array beyond basic research to include more clinically relevant scenarios, such as patient-specific drug screening or real-time monitoring of tissue-engineered constructs, could significantly enhance its utility. Collaborations with clinical researchers and industry partners could facilitate the translation of this technology into routine clinical practice, potentially revolutionizing the way we assess tissue mechanics and drug efficacy in personalized medicine.

Moreover, this system enables more comprehensive investigations of the tumor microenvironment. By incorporating key cell types involved in cancer progression, it facilitates fundamental studies of the underlying mechanisms of tumor development. The findings presented here highlight the potential of this platform for probing biophysical cues relevant to cancer research. In particular, the system offers a direct means to examine how cells and the ECM interact and collectively drive biophysical alterations within the tissue.

Therefore, while our high-throughput sensor array represents a major step forward in the field of mechanobiology, ongoing improvements in fabrication techniques, model complexity, and clinical integration will be crucial to fully realize its potential in both research and clinical applications.

5. Discussion

The high-throughput sensor array provides versatile and scalable technology to probe mechanobiology, particularly in the context of healthy or diseased tissues reliant on cellular forces and matrix mechanics. This innovation addresses long-standing challenges in quantifying the forces exerted by cells or tissue constructs *in vitro*, as well as assessing the dynamic remodeling of the cell-matrix environment. By leveraging micro-milling techniques to fabricate low-cost, scalable, and versatile PDMS molds, we have created a system that not only facilitates high-throughput experiments but also holds the potential for integration into clinical settings, such as drug screening protocols. The sensor array's ability to generate multiple 3D samples simultaneously within a single dish enhances the experimental throughput, while the cost-effectiveness and time efficiency of micro-milling make it an attractive alternative to more expensive and time-consuming lithographic techniques. Additionally, the capacity to create deeper, 3D structures with variable depths, without requiring multiple processing steps, provides a level of versatility that is particularly valuable for complex tumor modeling.

However, there are limitations inherent to the current micro-milling technology that must be addressed. The precision and resolution achievable with micro-milling, while similar to 3D printing, do not yet match the ultra-high precision offered by DRIE, especially for applications requiring micrometer-scale features. The challenges associated with using smaller-sized endmills, including tool wear, breakage, and thermal distortion of PMMA molds, further highlight the need for ongoing refinement of the fabrication process. Future research should focus on optimizing these processes, possibly through the integration of hybrid fabrication techniques that combine the strengths of micro-milling with other high-resolution methods. Nonetheless, regardless of the specific fabrication strategy employed or the used material, the development of a versatile high-throughput sensor array remains critical for advancing mechanobiology and enabling systematic, clinically relevant studies in 3D tumor models.

It is important to mention that PDMS has a well-documented absorption and adsorption characteristics which should be considered when using PDMS for device fabrication. These interactions can influence local drug concentration, diffusion and assay readouts if not carefully controlled [48]. To minimize these effects, all PDMS layers within each device should be produced using an identical and carefully controlled fabrication protocol, ensuring that any material-related properties remained uniform across the device. Additionally, consistency should be maintained in the application of drugs and reagents to reduce variability associated with the inherent absorption/adsorption behavior of PDMS.

In terms of impact, the potential applications of this sensor array extend far beyond fundamental research. Our results in the successful demonstration of its use with patient-derived cancer organoids underscore its utility in faithfully modeling tumor-stroma interactions in 3D and in individualized drug efficacy testing. This was exemplified in studies with ATRA, which effectively reverses PSC-induced matrix stiffening by reducing contractility and enhancing proteolytic remodeling, thereby normalizing the tumor microenvironment [39]. These findings open the possibility of reducing matrix stiffness with ATRA to enhance tissue permeability and amplify the efficacy of chemotherapy when used in combination. While promising, this hypothesis warrants further investigation to validate its therapeutic potential. The ability to assess mechanobiological responses in real time within 3D tumor models presents a powerful tool for personalized medicine, offering insights that could guide therapeutic decision-making. Consequently, our high-throughput sensor array represents a promising

advance for both research and clinical applications in the emerging field of mechanobiology.

6. Materials and methods

6.1. Cell culture

Human (PSCs, ScienCell Cat# 3830) were cultured in Stellate Cell Medium (SteCM, Cat #5301) as previously described by Haque *et al* [43]. Cells were grown at 37 °C in a humidified incubator with 5% CO_2.

The MIA PaCa-2 cell line was received as a gift from the Paul J. Hergenrother lab at the Department of Chemistry, University of Illinois Urbana-Champaign. The transfected MIA PaCa-2 cells used for fluorescence imaging were purchased from ATCC (Cat# CRL-1420) and subsequently transfected with tdTomato.

MIA PaCa-2 cells were grown in a high-glucose Dulbecco's Modified Eagle's Medium (DMEM) (Corning, Cat#: 10–013) supplemented with 10% FBS (Gibco, Cat#: A5670701) and 1% Penicilin/Streptomycin (Gibco, Cat#: 15 140 122).

6.2. Fabrication and assembly of PDMS sensors

The sensors were cast from micro-milled PMMA molds. These molds were designed in Fusion 360, and *G*-code was generated for milling them from clear PMMA. 6 mm thick scratch- and UV-resistant PMMA sheets (McMaster-Carr) were machined with a micro-end mill (Harvey Tool, USA) with a cutter diameter and length of cut of about 0.508 mm and 1.524 mm, respectively. A desktop computer numerical control (CNC) machine (Bulkman 3D Ultimate Bee) equipped with precision ball screws and driven by four closed-loop stepper motor using GRBL Mega v1.1 motion control firmware [49] was employed for this task. 24 000 rev min^{-1} spindle speed was used along with a maximum feed rate of 45.72 cm min^{-1} for positioning after manual collet adjustment to minimize tool runout. The dimensions of the machined cross-sections were measured using ImageJ software.

PDMS (Sylgard 184) was prepared by mixing the base and cross-linker at a 10:1 ratio by weight. Next, PDMS was pipetted into the molds, allowed to fill all the features and trenches by capillary micromolding [50], and then cured at 60 °C for 24 h. Using sharp tweezers, these device components were carefully peeled off the molds. For assembling the setup, the three layers of the device were joined by uncured PDMS, ensuring minimal air entrapment and a proper seal. Next, the assembled part was autoclaved, treated with 2% (v/v in ethanol) APTES (Sigma-Aldrich) for 12 h (and three times wash in ethanol after) and 0.5% (w/v in water) glutaraldehyde (Electron Microscopy Sciences) for 1 h (and 3× wash in water after). This part was then dried and glued to a large microscope slide (Ted Pella) using uncured PDMS. The device was ready to use after the PDMS glue was cured at 60 °C.

6.3. Tissue formation

High-concentration rat-tail collagen I (Corning, Cat#: 354249) solution was prepared on ice by neutralizing 9.5 mg ml^{-1} stock with 1 N sodium hydroxide, 10× PBS, and deionized water with proportions recommended in Corning protocol [51] to achieve a concentration of 4 mg ml^{-1} ECM with pH 7.2. The tissue precursor solution was prepared by mixing cell suspension (in media) with collagen at a 1:1 ratio to achieve a final collagen concentration of 2 mg ml^{-1} and cell density of 150 × 10^3 cells ml^{-1}. This density results in <10 cells in the tissue. To produce a higher number of cells, we increased density linearly based on the desired number of cells in the final tissue construct. For this study, we used 1.32 million Cells ml^{-1} and 0.66 million cells ml^{-1} for MIA PaCa-2 and PSCs, respectively.

Next, cell-ECM mixture was pipetted onto the grips of the sensors, and a capillary bridge was formed. With time, the solution filled the channels in the grips and polymerized at 37 °C for 45 min. It is important to add a small volume of media to the corners of each well before forming tissues, to prevent drying of tissues. After polymerization, culture media was carefully added to the wells with sensors so that the assembled tissues were inundated and then the array was placed in the incubator or microscope for experimentation.

Matrigel (Corning, Cat#: 354237) was incorporated in selected experiments. In these cases, the cell suspension in culture medium was combined with Matrigel to achieve a concentration of 2 mg ml^{-1}. The resulting cell-Matrigel suspension was subsequently mixed with collagen at a 1:1 ratio, resulting in a final concentration of 1 mg ml^{-1} for Matrigel.

6.4. Chemicals and drugs

Gemcitabine (MedChemExpress, Cat #: HY-17026) was reconstituted in dimethyl sulfoxide (DMSO) to a stock concentration of 10 mm and stored at −80 °C until use. ATRA (Sigma, Cat#: R2625) was prepared similarly in DMSO at 10 mm and maintained at −80 °C until experimental application.

6.5. IC_{50} determination, cell viability, and microplate reading

The IC_{50} assay was conducted using CellTiterGlo-3D by seeding 5000 MIA PaCa-2 cells and 5000 PSCs per well in 96-well opaque plates, followed by 48 h treatment with serial dilutions of Gemcitabine and ATRA at the following concentrations—50 μM, 10 μM, 2 μM, 400 nM, 80 nM, and 16 nM. Next, all the samples were incubated with the Cell-TiterGlo-3D (at 1:1 ratio of Medium to CellTiter-Glo-3D) for 30 min and then the luminescence (indicator of viability) was recorded on the GloMax Explorer

(Promega Corporation). Based on the luminescence, dose-response curves were plotted (figures 5(A) and (B)) and we determined an IC_{50} of 250 nM for Gemcitabine in MIA PaCa-2 cells and 12.5 μM for ATRA in PSCs.

To evaluate the effect of the combination treatment of Gemcitabine + ATRA (both at their IC50 concentrations) on the different cell lines (monoculture), we seeded 10 wells containing 3300 MIA PaCa-2 cells and treated them with Gemcitabine + ATRA. In parallel, we seeded ten wells containing 1600 PSCs and treated them with the same drug combination. For each monoculture condition, ten additional wells at the same cell densities were maintained as untreated controls. CellTiter-Glo3D luminescence signal reduction was quantified after 48 h of treatment by applying the CellTiter-Glo3D reagent in 1:1 (Medium:CellTiterGlo-3D) ratio (figure 5(C)).

To evaluate the effect of the combination treatment of Gemcitabine + ATRA on the co-culture of MIA PaCa-2 and PSC, we prepared 10 samples consisting of 3,300 MIA PaCa-2 cells + 1600 PSCs and treated them with Gemcitabine + ATRA at their IC_{50} concentrations, with ten untreated co-culture samples serving as controls. CellTiter-Glo3D luminescence signal reduction was quantified after 48 h of treatment, by applying the CellTiter-Glo3D reagent in 1:1 (Medium:CellTiterGlo-3D) ratio.

For quantifying the viability of cells in 3D, tissues were formed on the micro-array devices, resulting in 8 samples per each drug regimen, using two micro-array devices in parallel. The tissues were allowed to compact and remodel the matrix for the first 24 h. The tissues were then treated with Gemcitabine, ATRA, and Gemcitabine + ATRA, all at their IC_{50} concentrations, with 8 samples being kept as controls and not treated with any drugs. For viability measurement, 3D tissues were incubated with the reagent at a 1:1 ratio (Medium: CellTiter Glo3D reagent) and shaken for 30 min. The supernatant was then transferred to an opaque-walled plate, and luminescence was recorded on the GloMax Explorer (Promega Corporation).

6.6. PDAC organoids

PDOs was generated as described in previous studies [43, 52]. Organoids were generated from biopsies of untreated pancreatic cancer tissue at Rush University Medical Center. In brief, the biopsy tissues were digested using collagenase II, Dispase II, and DNase I, then washed multiple times. They were subsequently plated in 50 μl Matrigel domes on a 24-well plate with 500 μl of organoid medium. The growth medium consisted of Advanced DMEM/F12, N2 Supplement, N-acetyl cysteine, B27, PGE2, HEPES, nicotinamide, gastrin, hEGF, A83-01, Y-27 632, hFGF, and Wnt3A–R-spondin 1–Noggin conditioned media (50% of the final volume).

6.7. Imaging

The experiment was run in an environment-controlled chamber enclosing an inverted optical microscope (Olympus IX81, 10X objective, Olympus) mounted on a vibration isolation table (Newport Corporation). The chamber maintains cell culture conditions at 37 °C temperature, 5% CO_2 and 70% humidity. Moreover, a motorized stage (Prior Scientific Inc.) was programmed to track multiple specimens at preset locations at multiple time points. Images of both the tissues were acquired in BF mode with a Neo sCMOS camera (Andor Technology). For calculating spring displacements, images of the sensor gauges were analyzed using a template matching plugin in ImageJ with sub-pixel resolution. Force and stiffness calculations were made from the spring displacements, according to a previously described protocol [14].

SHG images were acquired subsequently using a LSM 710 (Zeiss) two-photon excitation microscope and 20X objective lens. Maximum intensity projection of the acquired confocal z-stacks was constructed using the ImageJ (U.S. National Institutes of Health) software.

Fluorescence microscopy of the 3D cancer tissue constructs was performed using a LSM 980 confocal microscope (Zeiss) equipped with a 20X objective lens.

6.8. Viability assessment of PDOs using the cancer-on-a-chip microfluidic system

PDOs were co-cultured with stromal PSCs on a microfluidic system [43]. Tumors were treated for 48 h with one of the following conditions: (i) controls; (ii) Gemcitabine at its experimentally determined IC_{50}; or (iii) Gemcitabine at IC_{50} combined with ATRA also at its IC_{50}. Following treatment, cultures were fixed and stained for EpCAM to label epithelial tumor cells and c.c.3 to identify apoptotic cells. For each well, multiple independent fields of views were imaged. Quantification of epithelial apoptosis was calculated as the ratio of $c.c.3^+$ cells to total $EpCAM^+$ cells.

6.9. Statistics and reproducibility

Data are presented as mean ± standard deviation (SD) unless otherwise stated. Statistical analyzes were performed using standard parametric tests. For comparisons involving more than two groups, one-way analysis of variance (ANOVA) was used to assess overall differences among group means. When the ANOVA indicated statistical significance, post hoc pairwise comparisons were performed using Fisher's least significant difference (LSD) test. For comparisons between two groups, either Student's t-test or Welch's t-test was applied, depending on variance homogeneity. A p-value of less than 0.05 was considered statistically significant. Statistical significance

of pairwise means comparison is provided in table S1-5 (supplementary information). All statistical analyzes and graphical representations were performed using OriginPro 2025b.

For mechanical characterization of tissue constructs, three independent experimental replicates were performed. For each experimental condition (control, Gemcitabine-treated, ATRA-treated, and combined Gemcitabine + ATRA), a minimum of nine valid samples were included in the final analysis. For PDO experiments, all samples from two independent microarray devices were analyzed, including eight control samples, eight Gemcitabine-treated samples, eight ATRA-treated samples, and eight Gemcitabine + ATRA treated samples. All experiments were repeated independently, and consistent results were obtained across replicates.

Acknowledgments

Research reported in this publication was partially supported by NSF Grants ECCS 1934991 and CMMI 2342257, Cancer Center at Illinois (CCIL) seed grant, and the Chan Zuckerberg Biohub Chicago. F B would like to acknowledge NIH support, CA27948, CA277110 and AG086145. K C S and M H R were supported by the U.S. Office of Naval Research (Award No. N00014-22-1-2577).

Data availability statement

All data that support the findings of this study are included within the article (and any supplementary files).

Supplementary information available at https://doi.org/10.1088/1758-5090/ae5347/data1.

Ethical Statement

We confirm that this current study is adherent to the IRB approval, informed consent, and the Declaration of Helsinki.

Conflict of interest

The authors declare that they have no competing interest.

Author contributions

Bashar Emon 0000-0002-5211-8014
Conceptualization (lead), Data curation (lead), Formal analysis (lead), Investigation (equal), Methodology (lead), Visualization (equal), Writing – original draft (lead), Writing – review & editing (lead)

Ahmadreza Kashefi 0009-0003-1764-3838
Conceptualization (equal), Data curation (equal), Formal analysis (equal), Investigation (equal), Methodology (equal), Writing – original draft (equal)

Md Habibur Rahman 0000-0003-1936-1917
Methodology (equal), Writing – original draft (equal)

Darbaz Adnan
Methodology (equal), Visualization (supporting)

Natalia Ospina-Munoz
Methodology (supporting)

Seamus M Mellican
Methodology (supporting)

Sophia Santiago
Methodology (supporting)

William C Drennan
Investigation (supporting), Methodology (equal)

Md Saddam Hossain Joy 0000-0001-5555-2222
Methodology (equal), Visualization (equal)

Aja A Phan 0009-0007-0451-8316
Methodology (equal)

Tasmia Afrin
Writing – original draft (supporting)

Luca S Santovito 0009-0004-0807-3893
Investigation (supporting)

Bumsoo Han
Funding acquisition (equal), Writing – review & editing (equal)

Kyle C Smith
Funding acquisition (equal), Writing – review & editing (equal)

Faraz Bishehsari
Conceptualization (equal), Funding acquisition (equal), Writing – review & editing (equal)

M Taher A Saif 0000-0003-2152-5116
Conceptualization (lead), Funding acquisition (lead), Supervision (lead), Writing – review & editing (lead)

References

[1] Rauner G, Gupta P B and Kuperwasser C 2025 From 2D to 3D and beyond: the evolution and impact of *in vitro* tumor models in cancer research *Nat. Methods* **22** 1–12

[2] Abuwatfa W H, Pitt W G and Husseini G A 2024 Scaffold-based 3D cell culture models in cancer research *J. Biomed. Sci.* **31** 1–39

[3] Peng Z, Lv X, Sun H, Zhao L and Huang S 2025 3D tumor cultures for drug resistance and screening development in clinical applications *Mol. Cancer* **24** 1–16

[4] Sheth M, Sharma M, Lehn M, Reza H A, Takebe T, Takiar V, Wise-Draper T and Esfandiari L 2024 Three-dimensional matrix stiffness modulates mechanosensitive and phenotypic alterations in oral squamous cell carcinoma spheroids *APL Bioeng.* **8** 36106

[5] Micalet A, Moeendarbary E and Cheema U 2021 3D *in vitro* models for investigating the role of stiffness in cancer invasion *ACS Biomater. Sci. Eng.* **9** 3729–41

[6] Zaman M H, Trapani L M, Siemeski A, MacKellar D, Gong H, Kamm R D, Wells A, Lauffenburger D A and Matsudaira P 2006 Migration of tumor cells in 3D matrices is governed by matrix stiffness along with cell-matrix adhesion and proteolysis *Proc. Natl Acad. Sci. USA* **18** 10889–94 (Accessed 14 September 2025)

[7] Nerger B A, Siedlik M J and Nelson C M 2017 Microfabricated tissues for investigating traction forces involved in cell migration and tissue morphogenesis *Cell. Mol. Life Sci.* **74** 1819–34

[8] Del Álamo J C, Meili R, Álvarez-González B, Alonso-Latorre B, Bastounis E, Firtel R and Lasheras J C 2013 Three-dimensional quantification of cellular traction forces and mechanosensing of thin substrata by fourier traction force microscopy *PLoS One* **8** e69850

[9] Hayn A, Fischer T and Mierke C T 2020 Inhomogeneities in 3D collagen matrices impact matrix mechanics and cancer cell migration *Front. Cell Dev. Biol.* **8** 593879

[10] Polackwich R J, Koch D, Arevalo R, Miermont A M, Jee K J, Lazar J, Urbach J, Mueller S C and McAllister R G 2013 A novel 3D Fibril force assay implicates src in tumor cell force generation in collagen networks *PLoS One* **8** e58138

[11] Böhringer D *et al* 2024 Dynamic traction force measurements of migrating immune cells in 3D biopolymer matrices *Nat. Phys.* **20** 1816–23

[12] Steinwachs J, Metzner C, Skodzek K, Lang N, Thievessen I, Mark C, Münster S, Aifantis K E and Fabry B 2016 Three-dimensional force microscopy of cells in biopolymer networks *Nat. Methods* **13** 171–6

[13] Emon B, Li Z, Joy M S H, Doha U, Kosari F and Saif M T A 2021 A novel method for sensor-based quantification of single/multicellular force dynamics and stiffening in 3D matrices *Sci. Adv.* **7** eabf2629

[14] Emon B, Joy M S H, Drennan W C and Saif M T A 2025 A multi-functional sensor for cell traction force, matrix remodeling and biomechanical assays in self-assembled 3D tissues in vitro *Nat. Protoc.* **20** 2005–33

[15] Eikanger M M, Schraufnagel K S, Slunecka J L, Potts R A, Freeling J, Brockstein R L, Emon B, Saif M T A and Rezvani K n.d. Veratridine, a plant-derived alkaloid, suppresses the hyperactive Rictor-mTORC2 pathway: a new targeted therapy for primary and metastatic colorectal cancer *Res. Sq.* rs–3

[16] Emon B, Joy M S H, Lalonde L, Ghrayeb A, Doha U, Ladehoff L, Brockstein R, Saengow C, Ewoldt R H and Saif M T A 2024 Nuclear deformation regulates YAP dynamics in cancer associated fibroblasts *Acta Biomater.* **173** 93–108

[17] Hossain Joy M S, Nall D L, Emon B, Lee K Y, Barishman A, Ahmed M, Rahman S, Selvin P R and Saif M T A 2023 Synapses without tension fail to fire in an in vitro network of hippocampal neurons *Proc. Natl Acad. Sci. USA* **120** e2311995120

[18] Legant W R, Pathak A, Yang M T, Deshpande V S, McMeeking R M and Chen C S 2009 Microfabricated tissue gauges to measure and manipulate forces from 3D microtissues *Proc. Natl Acad. Sci. USA* **106** 10097–102

[19] Guckenberger D J, De Groot T E, Wan A M D, Beebe D J and Young E W K 2015 Micromilling: a method for ultra-rapid prototyping of plastic microfluidic devices *Lab Chip* **15** 2364–78

[20] Serje D, Pacheco J and Diez E 2020 Micromilling research: current trends and future prospects *Int. J. Adv. Manuf. Technol.* **111** 1889–916

[21] Balázs B Z, Geier N, Takács M and Davim J P 2020 A review on micro-milling: recent advances and future trends *Int. J. Adv. Manuf. Technol.* **112** 655–84

[22] Elhebeary M, Emon M A B, Aydin O and Saif M T A 2019 A novel technique for *in situ* uniaxial tests of self-assembled soft biomaterials *Lab Chip* **19** 1153–61

[23] Emon B, Bauer J, Jain Y, Jung B and Saif T 2018 Biophysics of tumor microenvironment and cancer metastasis—A mini review *Comput. Struct. Biotechnol. J.* **16** 279–87

[24] Bauer J, Emon M A B, Staudacher J J, Thomas A L, Zessner-Spitzenberg J, Mancinelli G, Krett N, Saif M T and Jung B 2020 Increased stiffness of the tumor microenvironment in colon cancer stimulates cancer associated fibroblast-mediated prometastatic activin A signaling *Sci. Rep.* **10** 1–11

[25] Rice A J, Cortes E, Lachowski D, Cheung B C H, Karim S A, Morton J P and Del Río Hernández A 2017 Matrix stiffness induces epithelial–mesenchymal transition and promotes chemoresistance in pancreatic cancer cells *Oncogenesis* **6** e352

[26] Drifka C R, Loeffler A G, Mathewson K, Keikhosravi A, Eickhoff J C, Liu Y, Weber S M, Kao W J and Eliceiri K W 2016 Highly aligned stromal collagen is a negative prognostic factor following pancreatic ductal adenocarcinoma resection *Oncotarget* **7** 76197

[27] Rubiano A, Delitto D, Han S, Gerber M, Galitz C, Trevino J, Thomas R M, Hughes S J and Simmons C S 2018 Viscoelastic properties of human pancreatic tumors and in vitro constructs to mimic mechanical properties *Acta Biomater.* **67** 331–40

[28] Tetrick M G, Emon M A B, Doha U, Marcellus M, Symanski J, Ramanathan V, Saif M T A and Murphy C J 2025 Decoupling chemical and mechanical signaling in colorectal cancer cell migration *Sci. Rep.* **15** 1–14

[29] Raub C B, Suresh V, Krasieva T, Lyubovitsky J, Mih J D, Putnam A J, Tromberg B J and George S C 2007 Noninvasive assessment of collagen gel microstructure and mechanics using multiphoton microscopy *Biophys. J.* **92** 2212–22

[30] Emon B, Song Y J, Joy M S H, Kovour M V, Prasanth K V and Saif M T A 2023 Mechanosensitive changes in the expression of genes in colorectal cancer-associated fibroblasts *Sci. Data* **10** 1–6

[31] Bell C C *et al* 2018 Ingelman-sundberg, comparison of hepatic 2D sandwich cultures and 3D spheroids for long-term toxicity applications: a multicenter study *Toxicol. Sci.* **162** 655–66

[32] Jensen C and Teng Y 2020 Is it time to start transitioning from 2D to 3D cell culture? *Front. Mol. Biosci.* **7** 513823

[33] Imamura Y *et al* 2015 Comparison of 2D- and 3D-culture models as drug-testing platforms in breast cancer *Oncol. Rep.* **33** 1837–43

[34] Del M.b. Garnique A, Parducci N S, de Miranda L B L, de Almeida B O, Sanches L and Machado-Neto J A 2024 Two-dimensional and spheroid-based three-dimensional cell culture systems: implications for drug discovery in cancer *Drugs Drug Candidates* **3** 391–409

[35] Kanari M *et al* 2025 A three-dimensional ex vivo model recapitulates *in vivo* features and drug resistance phenotypes in childhood acute lymphoblastic leukemia *Leukemia* **39** 1–14

[36] Kocher H M *et al* 2025 Study protocol: multi-centre, randomised controlled clinical trial exploring stromal targeting in locally advanced pancreatic cancer; STARPAC2 *BMC Cancer* **25** 1–8

[37] Bi G, Liang J, Bian Y, Shan G, Besskaya V, Wang Q and Zhan C 2023 The immunomodulatory role of all-trans retinoic acid in tumor microenvironment *Clin. Exp. Med.* **23** 591–606

[38] Kocher H M *et al* 2020 Phase I clinical trial repurposing all-trans retinoic acid as a stromal targeting agent for pancreatic cancer *Nat. Commun.* **11** 1–9

[39] Chronopoulos A et al 2016 ATRA mechanically reprograms pancreatic stellate cells to suppress matrix remodelling and inhibit cancer cell invasion *Nat. Commun.* **7** 1–12
[40] Burris H A et al 2023 Improvements in survival and clinical benefit with gemcitabine as first-line therapy for patients with advanced pancreas cancer: a randomized trial *J. clin. oncol.* **41** 5482–92
[41] Heinemann V and Grosshadern K 2000 Gemcitabine: progress in the treatment of pancreatic cancer *Oncology* **60** 8–18
[42] Heinemann V, Wilke H, Mergenthaler H G, Clemens M, König H, Illiger H J, Arning M, Schalhorn A, Possinger K and Fink U 2000 Gemcitabine and cisplatin in the treatment of advanced or metastatic pancreatic cancer *Ann. Oncol.* **11** 1399–403
[43] Haque M R, Wessel C R, Leary D D, Wang C, Bhushan A and Bishehsari F 2022 Patient-derived pancreatic cancer-on-a-chip recapitulates the tumor microenvironment *Microsyst. Nanoeng.* **8** 1–13
[44] Armstrong A, Haque M R, Mirbagheri S, Barlass U, Gilbert D Z, Amin J, Singh A, Naqib A and Bishehsari F 2021 Multiplex patient-based drug response assay in pancreatic ductal adenocarcinoma *Biomedicines* **9** 705
[45] Huff M, Romano L and Jefimovs K 2021 Recent advances in reactive ion etching and applications of high-aspect-ratio microfabrication *Micromachines* **12** 991
[46] Gerlt M S, Läubli N F, Manser M, Nelson B J and Dual J 2021 Reduced etch lag and high aspect ratios by deep reactive ion etching (Drie) *Micromachines* **12** 542
[47] Advanced Output Center Formlabs design specifications - SAIC advanced output center n.d. (available at: https://sites.saic.edu/aoc/formlabs-design-specifications/) (Accessed 10 December 2024)
[48] Ramos I, Gonçalves M, Gonçalves I M, Carvalho V, Fernandes E, Lima R and Pinho D 2025 PDMS surface wettability modification and its applications: a systematic review *J. Mol. Liq.* **434** 127978
[49] Jeon S GitHub - gnea/grbl-mega: an open source, embedded, high performance g-code-parser and CNC milling controller written in optimized C that will run on an arduino mega2560 (available at: https://github.com/gnea/grbl-Mega) (Accessed 21 March 2024)
[50] Rajagopalan J and Saif M T A 2013 Fabrication of freestanding 1-D PDMS microstructures using capillary micromolding *J. Microelectromech. Syst.* **22** 992–4
[51] Corning Incorporated n.d. Certificate of analysis for corning collagen I high concentration (HC) Rat Tail (available at: https://certs-ecatalog.corning.com/life-sciences/certs/354236/354236_6207007.pdf) (Accessed 4 July 2020)
[52] Sharma D, Adnan D, Abdel-Reheem M K, Anafi R C, Leary D D and Bishehsari F 2024 Circadian transcriptome of pancreatic adenocarcinoma unravels chronotherapeutic targets *JCI Insight* **9** e177697